Chapter 17
Homogeneous Nucleation of Smoke Particles and Its Relationship with Cosmic Dust Particles

Yuki Kimura and Katsuo Tsukamoto

17.1 Nucleation of Cosmic Dust Particles

In the universe, most atoms exist in the gas phase and only about 1 % of atoms are incorporated into solid materials known as "cosmic dust particles" or simply "dust" or "grain." Despite its comparatively low abundance, cosmic dust is very important, because it forms the building material for planetary systems, acts as a substrate for the formation of molecules, and controls the energy balance in astronomical environments. Our main motivation is to understand the life cycle of materials in relation to the life cycles of stars. Knowledge of the initial state of the materials is essential for modeling of their subsequent evolution. The first solid materials were formed in gaseous ejecta from dying stars, such as asymptotic giant branch (AGB) stars or supernovae (Fig. 17.1). At this stage, no substrates were available for heterogeneous nucleation and, consequently, solid materials must have nucleated homogeneously. Homogeneous nucleation can only occur under conditions of significantly high supersaturation (Kimura et al. 2011, 2012; Kimura and Tsukamoto 2011). Under these conditions, the size of critical nuclei will be of the order of several nanometers or less. Once initial solid materials form, the

Y. Kimura (✉)
Institute of Low Temperature Science, Hokkaido University, Kita-19, Nishi-8, Kita-ku, 060-0819 Sapporo, Japan
e-mail: ykimura@lowtem.hokudai.ac.jp

K. Tsukamoto
Department of Earth and Planetary Materials Science, Graduate School of Science, Tohoku University, 980-8578 Sendai, Japan

Graduate School of Engineering, Osaka University, 565-0871 Suita, Osaka, Japan

A.E.S. Van Driessche et al. (eds.), *New Perspectives on Mineral Nucleation and Growth*,
DOI 10.1007/978-3-319-45669-0_17

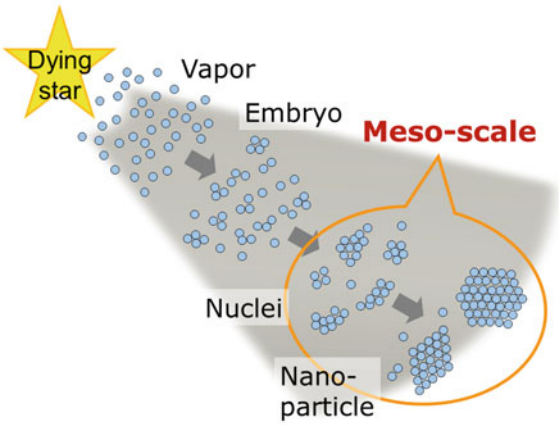

Fig. 17.1 Schematic showing the processes involved in the formation of cosmic particles in the gaseous outflow from a dying star. The size of cosmic dust particles must pass through the mesoscale to form dust with a size of the order of nanometers

remaining gaseous atoms have a much higher chance of undergoing heterogeneous nucleation on the nascent surface. Consequently, the initial nuclei govern the early stages of the growth process in the evolution of materials.

Small amounts of dust with an anomalous isotopic composition compared with solar minerals have been found in meteorites (Bernatowicz et al. 1991, 1996). Their composition suggests that they were formed before the birth of our solar system, and they are therefore referred to as "presolar grains." Spherules with a metal carbide core and a graphitic mantle are examples of presolar grains formed by heterogeneous nucleation on a primary grain. The graphitic spherules, which have a diameter of 0.43–4.2 μm and contain metal carbide crystals with a diameter of 7–90 nm, are assumed to have formed within the circumstellar envelopes of carbon-rich AGB stars (Croat et al. 2005). The metal carbide crystals, which consisted of Ti and/or Zr/Mo carbide, are generally located at the centers of individual spherules and are surrounded by well-graphitized carbon. It was therefore assumed that the metal carbide condensed before the carbon. On the basis of the condensation sequence and the sizes of the core and mantle, the conditions and environment for the formation of the grains, such as the total gas pressure, the carbon–oxygen ratio, the gas outflow velocity, and the stellar mass-loss rate, have been calculated by means of classical nucleation theory (Lodders and Fegley 1995; Sharp and Wasserburg 1995; Yamamoto and Hasegawa 1977; Draine and Salpeter 1977; Kozasa and Hasegawa 1987). However, it is difficult to explain the thickness of the graphitic mantle layer on the basis of the typical physical conditions expected in the circumstellar envelopes of carbon-rich AGB stars (Chigai et al. 2003).

Similarly, the processes involved in the formation of many other types of crystalline grains found in meteorites are unknown for reasons that might be associated with phenomena characteristic of nanoparticles and with the uncertainties associated with the physical properties of nanometer-sized particles (Kimura 2012). In the nucleation process, the size of particles passes through the mesoscale. Consequently, the physical properties and singular phenomena associated with

nanoparticles must be taken into account if we are to understand the nucleation process and the processes involved in the formation of cosmic dust particles.

17.2 Characteristic Phenomena in Nucleation

In nucleation, a free-energy barrier must be overcome for atoms or molecules to form bulk materials (e.g., Lutsko 2017, Chap. 2). The size of particles, once nucleated, must pass through the mesoscale. We believe that this produces one of the major difficulties in understanding the process of nucleation. For example, let us consider the growth of a nanoparticle consisting of 44 atoms. How many steps are required for this to grow twice its initial size? Usually, at each step, an atom from a mother phase will attach to the surface of the particle and will subsequently be incorporated stochastically into the particle. The next atom then comes from elsewhere and will similarly attach to the surface of the particle. By this route, 44 steps will be needed to double the size of the initial particle. However, nanoparticles can grow by another, shorter route that involves only two steps: attachment and diffusion (Fig. 17.2).

The latter growth mode, called fusion growth, can be seen in the micrographs recorded by in situ bright-field transmission electron microscopy (TEM) shown in Fig. 17.3. These micrographs show gold nanoparticles with a size of about 5 nm lying on the silica particle shown in the bottom right-hand corner of the

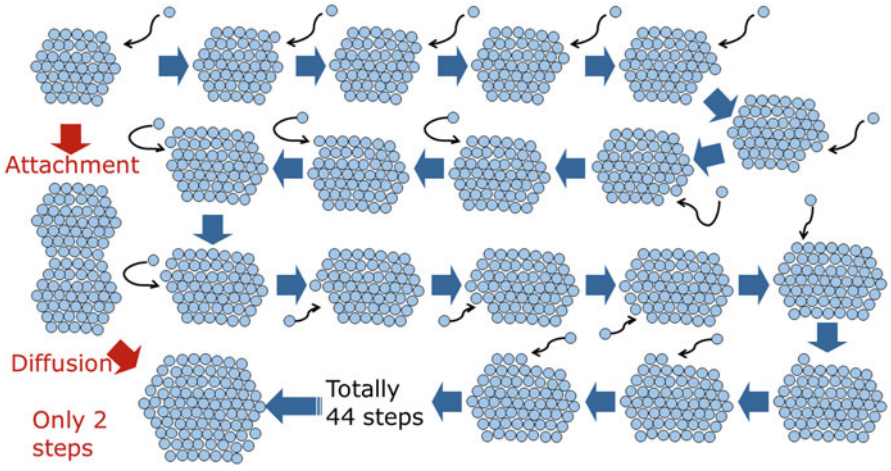

Fig. 17.2 Schematic showing two possible processes for the formation of nanoparticles. In the step-by-step process (classical model), shown by *gray arrows*, a nanoparticle grows by incorporation of individual growth units. In fusion growth, shown by *red arrows*, two nanoparticles coming into contact fuse to form a larger particle, thereby decreasing their total surface energy. Fusion growth is an example of a nonclassical model

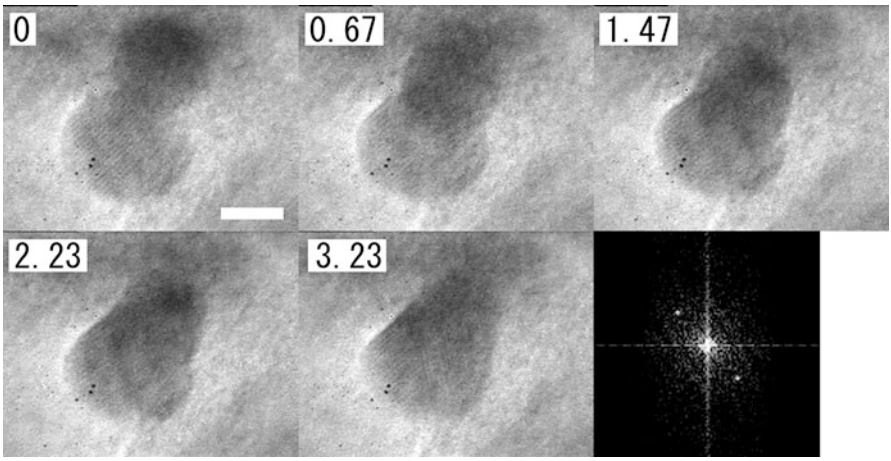

Fig. 17.3 Still micrographs of in situ bright-field TEM observations of an example of the fusion growth. The pictures are labeled with the time in seconds. Two gold particles migrate on the surface of the silica particle seen in the *bottom right-hand corner* in the images. When the two particles contact, they fuse together to decrease their total surface energy. The lattice fringes of the two gold nanoparticles indicate that the particles are crystalline. The final image shows a fast Fourier-transform (FT) diffraction pattern taken from the first image, confirming that the gold particles are crystalline. The *scale bar* corresponds to 3 nm

micrographs. Once the gold nanoparticles touch one another, they diffuse to form a larger particle, to decrease their total surface energy. This phenomenon is commonly experienced with water droplets. However, in this case, the gold nanoparticles show lattice fringes suggesting that they are crystalline. The diffusion constant of an atom in a nanoparticle is several orders of magnitude larger than that in the bulk material, provided that the diameter of the particle is less than 10 nm or so.

When a particle reaches a size of 10 nm, it will consist of about 10,000 atoms, more than 10 % of which are located on the surface of the particle. If we assume that the particle is spherical, the contribution of the surface energy compared with the total energy cannot be neglected. If the nucleation rate is significantly high, nuclei have a high chance of colliding with one another during, or just after, nucleation. The number density of the resulting particles will then decrease and become less than the value predicted by nucleation theory. For example, in the vapor-phase homogeneous nucleation of tungsten oxide, whereas the number density of the resulting particles is two orders of magnitude less than that predicted on the basis of the nucleation rate predicted by nucleation theory, the mass of the resulting particle is two orders of magnitude larger than the predicted value; in other words, the total mass is the same in the theoretical and experimental results (Kimura et al. 2011). This experiment suggests that hundreds of nuclei combined to form a particle during the nucleation process. The difference of several orders of magnitude between the experimental and the nucleation rate and that predicted by molecular-dynamics simulations and

nucleation theory is generally considered to be a limitation of nucleation theory (Schmitt et al. 1982; Adams et al. 1984; Feder et al. 1966; Yasuoka and Matsumoto 1998; Toxvaerd 2001, 2003). However, some of the difference between the actual formation rate and the calculated nucleation rate might be the result of fusion growth caused by the so-called size effects of nanoparticles. Therefore, characteristic phenomena of nanoparticles need to be taken into account to understand the process of formation of cosmic dust particles.

17.3 Smoke Experiments as Model Processes for Dust Formation

When a material evaporates in an inert gas, the evaporated hot vapor subsequently cools and nucleates to form nanoparticles that flow along with the convection current generated by the hot evaporation source. The flow resembles the smoke from a cigarette. Inside the chamber, because there is no substrate near the evaporation source, the particles nucleate homogeneously in a manner similar to cosmic dust particles. Although the gas around a dying star is much less dense than the experimental atmosphere, the presence of an inert gas decreases the mean free path of the evaporant. If materials are evaporated at similar pressures (below 10^{-4} Pa) to those surrounding a dying star, the evaporated vapor will collide directly with the surface of the chamber wall, because of the long mean free path (in excess of 10^3 m), and will form a thin film on it.

The presence of an inert gas also affects the nucleation conditions, particularly the relationship between the cooling rate and the collision frequency of the evaporated atoms or molecules. Yamamoto and Hasegawa (1977) proposed a nondimensional parameter Λ, defined by the timescale for supersaturation increase τ_{sat} and the collision frequency ν. Cosmic dust particles are formed in gaseous ejecta where the supersaturation gradually increases as the temperature decreases with distance from the central star. The parameter Λ is useful in discussing the characteristics of particles formed in a gaseous atmosphere consisting of various objects or even in the laboratory. In other words, particles formed under conditions with the same Λ value can be discussed similarly and should have similar characteristics. Typical Λ values for various objects and for various experiments are summarized in Table 17.1. This shows that dust in novae can be reproduced by laboratory experiments, and dust in supernovae and evolved stars can be reproduced by experiments performed in conditions of microgravity.

Table 17.1 Comparison of Λ values for natural and laboratory conditions

Object	Nova	Supernova	Evolved star	Solar system	Laboratory experiments	Microgravity experiments
Λ	10^0–10^2	10^4	10^3–10^6	10^9	10^0–10^2	10^2–10^4

Revision of Yamamoto and Hasegawa (1977)

17.4 In Situ Observation of Nucleation by Optical Methods

Nucleation is very difficult to visualize experimentally because it is a rapid process that occurs on a nanometer scale (e.g., Nielsen and De Yoreo 2017, Chap. 18). In contrast, direct observation of the nucleation environment is relatively easy and has been achieved by in situ measurements of temperatures, concentrations, and infrared (IR) spectra during nucleation from a vapor phase (Fig. 17.4); the temperatures and concentrations were measured by using a double-wavelength Mach–Zehnder-type interferometer, and the IR spectra were recorded by using an FT-IR spectrometer.

To produce nanoparticles by homogeneous nucleation from an evaporated vapor, the mean free path of the atmosphere must be reduced by the introduction of a buffer gas; this also permits the detection of the temperature and concentration of the evaporated vapor from the changes in its refractive index, as detected by an interferometer. Our experimental setup was capable of detecting a difference in refractive index of less than 1×10^{-6}, which, for example, corresponds to the difference in temperature from 298 K to 302 K for argon gas at 1×10^{4} Pa.

When a material is evaporated by electrical heating, changes in the refractive index are induced not only by variations in the temperature but also by variations in the concentration of the evaporated vapor. Because we used a double-wavelength Mach–Zehnder-type interferometer, operating at 532–635 nm, the temperature and the concentration could be determined by a simple calculation based on the displacement of the interference fringes at the two wavelengths and the total pressure, monitored by using a pressure gauge. The FT-IR spectrometer can distinguish the crystalline structure of free-flying nanoparticles during nucleation by means of spectra obtained in the region stretching from near the evaporation source to several centimeters above it.

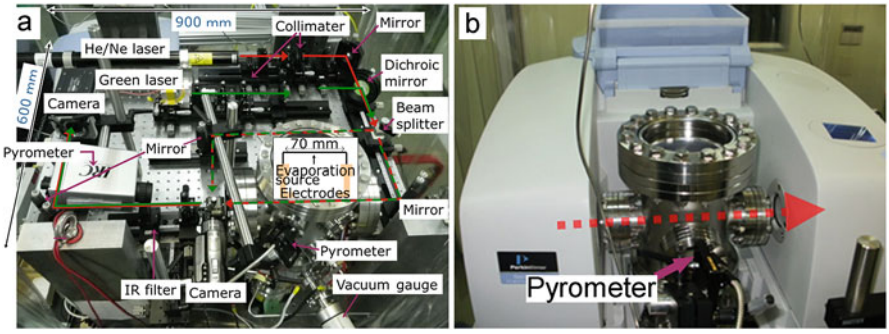

Fig. 17.4 (**a**) Photographs of (**a**) the experimental apparatus designed to produce nanoparticles that mimic cosmic dust together with the Mach–Zehnder-type interferometer and (**b**) the infrared spectrometer for in situ observation of the nucleation environment. The *red* and *green arrows* in (**a**) show the optical path of the interferometer. The *dotted arrow* in (**b**) shows the optical path of the infrared light

17.5 Interferometer Shows the Difficulty of Homogeneous Nucleation

Figure 17.5a is an example of an image of interference fringes before heating of the evaporation source. When the evaporation source was electrically heated, the interference fringes moved as a result of a decrease in the refractive index of the hotter surrounding argon gas (Fig. 17.5b). The refractive index of Ar, $n_{\mathrm{Ar(T,P)}}$, can be expressed as a function of temperature T (K) and pressure P_{Ar} (Pa) as follows:

$$n_{Ar(T,P)} - 1 = \frac{\left[n_{Ar(273.15,P_0)} - 1\right]}{1 + a\Delta T}\frac{P_{Ar}}{P_0} \tag{17.1}$$

where a is the coefficient of volume expansion (0.003663 K^{-1} in this experiment) and P_o is the pressure (101325 Pa). The shift in the fringes depends on the change in the optical path length L, which is defined as nl, where l is the physical length (70 mm in this experiment). The numbers of fringes of green (Δd_G) and red (Δd_R) that showed displacements from the positions of the starting interference fringes in Fig. 17.5a during heating are therefore given by the following equations:

$$\Delta d_G = \left[n_{GAr(Ti,Pi)} - n_{GAr(T,P_{Ar})} - n_{G_{E\left(T,P_E\right)}} + 1 \right] \frac{l}{\lambda_G} \tag{17.2}$$

and

$$\Delta d_R = \left[n_{RAr(Ti,Pi)} - n_{RAr(T,P_{Ar})} - n_{R_{E\left(T,P_E\right)}} + 1 \right] \frac{l}{\lambda_R} \tag{17.3}$$

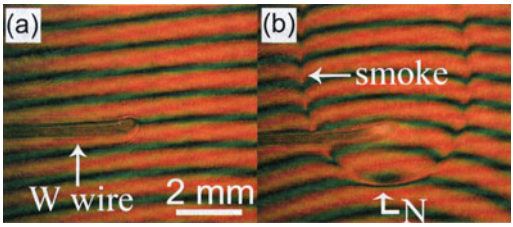

Fig. 17.5 Typical interference fringes taken along the longer axis of the tungsten wire with source temperatures of (**a**) room temperature and (**b**) ~1600 K in a mixture gas of argon (9.0×10^3 Pa) and oxygen (1.0×10^3 Pa). The tungsten wire was 0.3 mm in diameter and 70 mm long and it was oriented parallel to the optical path. The interference fringes in (**b**) suggest that homogeneous nucleation occurred around the evaporation source. Nucleated smoke particles flowed upward as a result of the convection current generated in the ambient gas

where T_i and P_i are the initial temperature and pressure before the temperature of the source was increased. The subscripts G and R show the values for the green and red lasers, respectively, and $P_{Ar} = P_{total} - P_E$, where P_E is the partial pressure of the evaporant. By using both equations, the temperature and concentration profiles can be determined simultaneously from the images in Fig. 17.5. The existence of nucleated particles can be confirmed in Fig. 17.5b, because the higher refractive index of solid particles produces the marked change in the interference fringes shown by the arrow labeled "smoke." Because of the rising convection current generated by the hot evaporation source, the evaporated vapor did not diffuse uniformly from the tungsten wire; instead, the rising tungsten oxide vapor was accelerated and downward flow of the vapor was restrained. As the result, a relatively high-concentration field was generated below the evaporation source compared in the same centric distance, i.e., the degree of supersaturation was highest to the direction below the evaporation source. Consequently, nucleation occurred below the evaporation source at the position shown by arrow N in Fig. 17.5b. The supersaturation ratio reached values as high as 10^7 for tungsten oxide and 10^4 for manganese. This high supersaturation was the result of homogeneous nucleation, because supersaturation does not increase to such high levels if heterogeneous nucleation would be occurred.

17.6 Determination of Physical Constants

The surface free energy and the sticking probability markedly affect the prediction by nucleation theory of the characteristics of a dust, such as its nucleation temperature, mineral species, size, and number density. The actual size of cosmic dust particles ranges from a few nanometers to around a hundred nanometers. Despite this, the surface free energy of the bulk material has always been used in calculations. Recent studies have, however, shown that the surface free energy of nanoparticle differs markedly from that of the bulk material. For example, in the case of rutile, which is a polymorph of titanium dioxide, the surface free energy of 14-nm-diameter particles is 30 % larger than that of the bulk material (Zhang et al. 2009). Because absolute values of the sticking probability are generally unknown, its value has often been assumed to be unity for the purposes of calculation. Actually, a higher sticking probability provides a better explanation of the amount of dust in the circumstellar environment. When a bulk experiment was performed to obtain the sticking probability for iron, it showed a value very close to unity (Tachibana et al. 2011). In the experiment, iron was evaporated onto a temperature-controlled iron substrate, and the mass of the evaporant and the adherent iron film were compared. In contrast, Michael et al. (2003) found a very low sticking probability of 10^{-5} in a nucleation experiment using zinc under microgravity conditions produced in a parabolic flight.

We also performed numerical simulations of the nonequilibrium condensation of several materials to determine their surface free energies and sticking coeffi-

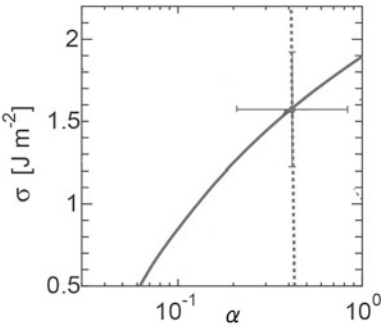

Fig. 17.6 A plot of the surface free energy σ against the sticking coefficient α, obtained by simulations using the SP nucleation model to explain the nucleation temperature (*solid line*) and the size of the resulting particles (*dashed line*) observed in experiments

cients. By in situ observations of a nucleation environment in conjunction with the application of nucleation theories, we succeeded in determining the surface free energies and sticking probabilities of nanoparticles undergoing homogeneous nucleation (Kimura et al. 2012). We considered a gaseous system that cools down with a specific timescale. By using this timescale, we calculated the equations governing the temporal evolution of the gas number density and the nucleation rate (Yamamoto and Hasegawa 1977; Tanaka et al. 2002). From these simulations, we obtain the condensation temperature and the size of the particles.

By comparing the results of the simulations with the experimental results, we were able to determine the surface fee energy and the sticking coefficient. Figure 17.6 shows possible values of the sticking coefficient α and the corresponding surface free energies σ that explain the nucleation temperature (solid line) and the size of the resulting particles (dashed line) from the experiments in terms of a semi-phenomenological (SP) nucleation model based on the results of experiments using Mn as an example. The crossing points are the surface free energy and sticking coefficient of Mn at 1106 ± 50 K, which are 1.57 ± 0.35 J m^{-2} and 0.4 (+0.42, –0.21), respectively. The error bar arises from variations in the partial pressure and timescale for cooling of Mn. Reported surface free energies of molten Mn include values of 1.1 J m^{-2} at 1573–1773 K (Turkdogan 1980) and 0.92–1.18 J m^{-2} at 1573 K (Shinozaki et al. 1998). The surface free energy of Mn nanoparticles is therefore about 30 % larger than that of molten Mn. We also performed a nucleation experiment with iron in a microgravity environment generated by using a sounding rocket. In this experiment, the sticking probability of iron was found to be as low as 10^{-4}, a value significantly lower than that of $\sim 10^{0}$ obtained by a ground-based bulk experiment (Tachibana et al. 2011).

17.7 Multistep Nucleation Processes

Homogeneous nucleation can only occur under conditions of very high supersaturation where the critical nuclei are only a few atoms in size. The melting point of a nanoparticle is generally lower than that of the corresponding bulk material

(Lee et al. 2009; Buffat and Borel 1976). In the case of Mn, the size of the critical nuclei is only 6 ± 1 atoms, as calculated from the SP model, due to the very large supersaturation. In the growth process of Mn nanoparticles from six atoms to their maximum size (13.7 nm in radius), the melting point will increase from about 800 K to 1519 K due to the size effects of the nanoparticles. Therefore, the initial structure of nascent Mn nanoparticles formed at 1106 ± 50 K can be regarded as being that of a liquid. Because of the size dependence of the melting point, supercooling of the molten Mn with respect to the melting point increases directly with increasing particle size, even if the temperature remains steady.

The particles that were formed consisted of mixtures of α-Mn and β-Mn, which are the stable phases at temperatures below 1015 K and between 1015 and 1368 K, respectively. The unit cells of α-Mn and β-Mn contain 58 and 20 atoms, respectively (JCPDS cards 32-637 and 33-887). Because the size of critical nuclei is much smaller than these values, the structure of the Mn nanoparticles is not determined at the point of nucleation. The polymorphism of the resulting Mn nanoparticles is therefore determined in the particle-growth phase and not in the vapor-to-liquid nucleation phase. This result confirms that the initial nucleation from the vapor phase does not control the resulting crystalline phase that eventually forms from the molten droplet. If that were the case, the crystal structure of the Mn nanoparticles would be determined when the crystal first nucleated homogeneously within the initial molten particle (second liquid–solid nucleation) rather than later in the growth phase. Both α-Mn and β-Mn nanoparticles can nucleate stochastically from the molten particles independently of the phase diagram; this is similar to the nucleation behavior of sodium chlorate (Kimura et al. 2014). Rapid cooling at more than 10^3 K s^{-1} may allow the preservation of the higher-temperature phase. This kind of two-step nucleation has also been reported in a molecular-dynamics simulation of the homogeneous condensation of argon vapor (Tanaka et al. 2011).

Infrared spectra recorded during the nucleation of magnesium silicate from a vapor phase also show the initial formation of a molten phase (Fig. 17.7). The initial single feature at 10 μm originates from amorphous or molten magnesium silicate. On cooling to about 500 K, the single feature becomes a double peak as a result of the presence of a crystalline phase. This crystallization is the result of supercooling of initially nucleated molten nanoparticles (Ishizuka et al. 2015). These studies for in situ observation of a nucleation environment are inchoate and will generate deeper insight and progress the understanding of nucleation in the coming decade.

17.8 Outlook

Using nucleation theories, we can calculate expected nucleation rates; however these rates are very different from those obtained by experiments or molecular-dynamics simulations. For instance, in the case of water or methanol nucleation from its vapor, the difference in nucleation rates is several orders. Hence, one of

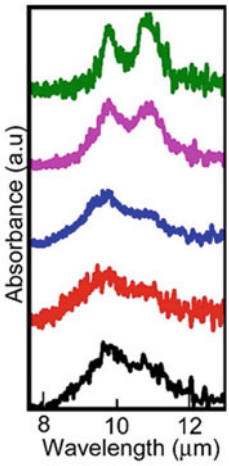

Fig. 17.7 Infrared spectra of magnesium silicate nanoparticles during nucleation recorded at distances of 2, 4, 6, 8, and 10 cm above the evaporation source (from the *bottom* to the *top*, respectively). The temperature decreases gradually above the evaporation source, and the crystallinity increases from less than 1 % at 2 cm to more than 20 % at 10 cm

the largest problems to understand nucleation is that we do not yet realize why nucleation rates are so different between theory and experiment or molecular-dynamics simulation. There are some possibilities, such as limitation of the theories, heterogeneous nucleation caused by not an ideal experiment, and occurrence of multistep nucleation. Nucleation from the vapor phase has the advantage that there is no water solution, which induces large hindrance during solution growth due to the dehydration process (e.g., DeYoreo et al. 2017, Chap. 1). In a water solution, both the crystals and growth units are usually surrounded by hydrated layers on their surfaces (Araki et al. 2014). Growth units have to eliminate/rearrange these hydrated layers before being incorporated into a crystal or nuclei. To do so, the system will try to find more thermodynamically favorable routes, which can eventually lead to "unexpected" nucleation processes.

Hence, before making a *super-unified* nucleation theory, first a more simple nucleation theory, applicable to the vapor phase, should be developed. In case of vapor-phase nucleation, binding energy of growth units seems more important than surface free energy, because a phenomenological nucleation theory, which takes into account the binding energy of a dimer, could reproduce nucleation rates in homogeneous nucleation experiments for some conditions (Kimura et al. 2012). Currently, these experiments have been performed using only one element. In the near future, we will perform these experiments for multicomponent systems, and then nucleation rates may be difficult to predict due to the occurrence of multistep nucleation events, even in a vapor phase. For instance, two different kinds of nanoparticles can merge to be a compound particle by fusion growth similarly with that shown in Fig. 17.3. Magnesium silicate (Mg_2SiO_4), which is an astronomically important mineral, may be able to form by a fusion growth of MgO and SiO_2 particles. A better understanding of the nucleation process should also provide us with new perspectives on material evolution in the universe.

References

Adams GW, Schmitt JL, Zalabsky RA (1984) The homogeneous nucleation of nonane. J Chem Phys 81:5074

Araki Y, Tsukamoto K, Takagi R, Miyashita T, Oyabu N, Kobayashi K, Yamada H (2014) Direct observation of the influence of additives on calcite hydration by frequency modulation atomic force microscopy. Cryst Growth Des 14:6254–6260

Bernatowicz TJ, Amari S, Zinner E et al (1991) Interstellar grains within interstellar grains. Astrophys J Lett 373:L73–L76

Bernatowicz TJ, Cowsik R, Gibbons PC et al (1996) Constraints on stellar grain formation from presolar graphite in the Murchison meteorite. Astrophys J 472:760–782

Buffat P, Borel J-P (1976) Size effect on the melting temperature of gold particles. Phys Rev A: At Mol Opt Phys 13:2287

Chigai T, Yamamoto T, Kaito C et al (2003) Are TiC grains a carrier of the 21 micron emission band observed around post–asymptotic giant branch objects? Astrophys J 587:771–776

Croat TK, Stadermann FJ, Bernatowicz TJ (2005) Presolar graphite from AGB stars: microstructure and *s*-process enrichment. Astrophys J 631:976–987

De Yoreo JJ, Sommerdijk NAJM, Dove PM (2017) Nucleation pathways in electrolyte solutions. In: Van Driessche AES, Kellermeier M, Benning LG, Gebauer D (eds) New perspectives on mineral nucleation and growth, Springer, Cham, pp 1–24

Draine BT, Salpeter EE (1977) Time-dependent nucleation theory. J Chem Phys 67:2230–2235

Feder J, Russell KC, Lothe I et al (1966) Homogeneous nucleation and growth of droplets in vapours. Adv Phys 15:111–178

Ishizuka S, Kimura Y, Sakon I (2015) In situ infrared measurements of free-flying silicate during condensation in the laboratory. Astrophys J 803:88

Kimura Y (2012) Phenomena of nanoparticles in relation to the solar system. In: Mann I, Meyer-Vernet N, Czechowski A (eds) Nanodust in the solar system: discoveries and interpretations. Springer, Heidelberg, pp 31–46

Kimura Y, Tsukamoto K (2011) Interferometric observation of temperature distributions in the smoke experiment. J Jpn Soc Microgravity Appl 28:S9–S12

Kimura Y, Miura H, Tsukamoto K, Li C, Maki T (2011) Interferometric in-situ observation during nucleation and growth of WO_3 nanocrystals in vapor phase. J Cryst Growth 316:196–200

Kimura Y, Tanaka KK, Miura H, Tsukamoto K (2012) Direct observation of the homogeneous nucleation of manganese in the vapor phase and determination of surface free energy and sticking coefficient. Cryst Growth Des 12:3278–3284

Kimura Y, Niinomi H, Tsukamoto K, García-Ruiz JM (2014) In situ live observation of nucleation and dissolution of sodium chlorate nanoparticles by transmission electron microscopy. J Am Chem Soc 136:1762

Kozasa T, Hasegawa H (1987) Grain formation through nucleation process in astrophysical environments II. Prog Theor Phys 77:1402–1410

Lee J, Lee J, Tanaka T et al (2009) In situ atomic-scale observation of melting point suppression in nanometer-sized gold particles. Nanotechnology 20:475706

Lodders K, Fegley B Jr (1995) The origin of circumstellar silicon carbide grains found in meteorites. Meteoritics 30:661–678

Lutsko JF (2017) Novel paradigms in nonclassical nucleation theory. In: Van Driessche AES, Kellermeier M, Benning LG, Gebauer D (eds) New perspectives on mineral nucleation and growth, Springer, Cham, pp 25–42

Michael BP, Nuth JA III, Lilleleht LU (2003) Zinc crystal growth in microgravity. Astrophys J 590:579–585

Nielsen MH, De Yoreo JJ (2017) Liquid phase TEM investigations of crystal nucleation, growth, and transformation. In: Van Driessche AES, Kellermeier M, Benning LG, Gebauer D (eds) New perspectives on mineral nucleation and growth, Springer, Cham, pp 353–371

Schmitt JL, Adams GW, Zalabsky RA (1982) Homogeneous nucleation of ethanol. J Chem Phys 77:2089–2097

Sharp C, Wasserburg G (1995) Molecular equilibria and condensation temperatures in carbon-rich gases. Geochim Cosmochim Acta 59:1633–1652

Shinozaki N, Sonoda M, Mukai K (1998) Wettability, surface tension, and reactivity of the molten manganese/zirconia–yttria ceramic system. Metall Mater Trans A 29:1121–1125

Tachibana S, Nagahara H, Ozawa K et al (2011) Kinetic condensation and evaporation of metallic iron and implications for metallic iron dust formation. Astrophys J 736(16):8

Tanaka KK, Tanaka H, Nakazawa K (2002) Non-equilibrium condensation in a primordial solar nebula: formation of refractory metal nuggets. Icarus 160:197–207

Tanaka KK, Tanaka H, Yamamoto T, Kawamura K (2011) Molecular dynamics simulations of nucleation from vapor to solid composed of Lennard–Jones molecules. J Chem Phys 134:204313

Toxvaerd S (2001) Molecular-dynamics simulation of homogeneous nucleation in the vapor phase. J Chem Phys 115:8913–8920

Toxvaerd S (2003) Molecular dynamics simulation of nucleation in the presence of a carrier gas. J Chem Phys 119:10764–10770

Turkdogan ET (ed) (1980) Physical chemistry of high temperature technology. Academic, New York

Yamamoto T, Hasegawa H (1977) Grain formation through nucleation process in astrophysical environment. Prog Theor Phys 58:816–828

Yasuoka K, Matsumoto M (1998) Molecular dynamics of homogeneous nucleation in the vapor phase. I. Lennard–Jones fluid. J Chem Phys 109:8451–8462

Zhang H, Chen B, Banfield JF (2009) The size dependence of the surface free energy of titania nanocrystals. Phys Chem Chem Phys 11:2553–2558